Computers & Geosciences 156 (2021) 104898

Contents lists available at ScienceDirect

Computers and Geosciences

journal homepage: www.elsevier.com/locate/cageo

SMART mineral mapping: Synchrotron-based machine learning approach for 2D characterization with coupled micro XRF-XRD

Julie J. Kim [a], Florence T. Ling [b], Dan A. Plattenberger [c], Andres F. Clarens [c], Antonio Lanzirotti [d], Matthew Newville [d], Catherine A. Peters [a,*]

[a] Department of Civil and Environmental Engineering, Princeton University, Princeton, NJ, 08544, USA
[b] Department of Chemistry, La Salle University, Philadelphia, PA, 19142, USA
[c] Engineering Systems and Environment, University of Virginia, Charlottesville, VA, 22904, USA
[d] Center for Advanced Radiation Sources, The University of Chicago, Chicago, IL, 60637, USA

ARTICLE INFO

Keywords:
Mineral mapping
Mineral spatial distribution
Synchrotron x-ray microprobe
X-ray fluorescence
Machine learning
Artificial neural network

ABSTRACT

A Synchrotron-based Machine learning Approach for RasTer (SMART) mineral mapping was developed for the purpose of training a mineral classifier for characterization of millimeter-sized areas of rock thin sections with micron-scale resolution. An Artificial Neural Network (ANN) was used to extract relationships between coupled micro x-ray fluorescence (μXRF) data for element abundances and micro x-ray diffraction (μXRD) data for mineral identity. Once trained, the resulting classifier, i.e., the SMART mineral mapper, can identify minerals using only μXRF data. This is the real value of this machine learning approach because μXRF data are relatively fast to collect and interpret whereas μXRD data take longer to collect and interpret. Training and testing of an initial mapper were done with 192 coupled μXRF-μXRD data points sampled from a 0.25 mm^2 area of a shale from the Eagle Ford formation, which was scanned with 2 μm resolution. All data used in this work were obtained from the Advanced Photon Source synchrotron beamline 13-ID-E at Argonne National Laboratory. Three minerals were mapped in the Eagle Ford rock sample, for which there were 8 elements characterized. In the testing phase, the minerals were correctly classified with accuracy of 97 % and higher. The trained SMART mapper was applied for self-similar upscaling by mapping a 14 mm^2 scan of the Eagle Ford sample. Generated maps captured micro-scale features characteristic of the stratified texture of the rock, and the identified minerals agreed well with bulk XRD analysis of the powdered rock. The SMART mapper was also applied to a scan of a 6-mineral mixture of known composition to demonstrate ability to distinguish minerals of similar chemistry. The trained SMART mapper is transferable to scans from other x-ray microprobes because of the μXRF data normalization that accounts for sample- and beamline-specific properties like thickness, detector configuration, and incident energy.

1. Introduction

Characterizations of mineral spatial distributions in highly heterogeneous rocks, sediments and synthetic materials are important in the fields of geosciences and environmental science and engineering. The ability to resolve spatial patterns of minerals at various scales is critical for characterizing properties such as porosity, permeability, texture, and fractures (Bensinger and Bekingham, 2020; Deng et al., 2015; Deng and Peters, 2019; Ellis et al., 2013; Ellis and Peters, 2016; Fitts and Peters, 2013; Glassley et al., 2002; Soulaine et al., 2016). More specifically in natural rocks and sediments, spatial knowledge of minerals is important for determining accessible mineral surface areas for mineral dissolution, and weathering reaction rate calculations (Beckingham et al., 2016; 2017; Deng et al., 2020; Li et al., 2017; Ma et al., 2019; Peters, 2009; Qin and Beckingham, 2019; Zhang et al., 2017), fluid adhesion on mineral surfaces (Wang et al., 2013), radionuclide or toxic metal (loid) mobilization (Ehlert et al., 2018; Kreisserman and Emmanuel, 2018; Robinet et al., 2012), and organic carbon cycles in soils (Basile-Doelsch et al., 2005). Furthermore, geomechanical and mechanical properties like unconfined compressive strength, or frictional strength of geologic formations, fractures or synthetic materials such as cements have also been found to be strongly dependent on mineral composition and

* Corresponding author. Department of Civil and Environmental Engineering, Princeton University, Princeton, NJ, 08544, USA.
E-mail address: cap@princeton.edu (C.A. Peters).

https://doi.org/10.1016/j.cageo.2021.104898
Received 23 December 2020; Received in revised form 3 July 2021; Accepted 26 July 2021
Available online 28 July 2021

distributions (Bourg, 2015; Fang et al., 2018; Gaboreau et al., 2017; Spokas et al., 2019).

Recent research has advanced benchtop and laboratory-based equipment and techniques in which elements and phases can be distinguished, quantified and spatially mapped. Such analytical and imaging techniques include optical microscopy imaging, electron probe microanalyzer (EPMA), x-ray computed tomography (xCT), scanning electron microscopy (SEM), backscattered electron (BSE) imaging, energy dispersive x-ray spectroscopy (EDS), laser-induced breakdown spectroscopy (LIBS), and micro energy dispersive x-ray fluorescence spectrometry (μ-EDXRF). Furthermore, researchers have developed novel ways of coupling these techniques to yield comprehensive, multimodal-based information about the minerals present and their spatial distributions within geologic samples (Deng et al., 2016; Ellis and Peters, 2016; Golab et al., 2013; Guntoro et al., 2019a, 2019b; Jennings-Gray et al., 2020; Maitre et al., 2019; Nikonow and Rammlmair, 2017; Nikonow et al., 2019; Pirrie et al., 2004; Pret et al., 2010; Rahman et al., 2016; Sutherland and Gottlieb, 1991; Tsuji et al., 2010). Also worth mentioning are commercially available software tools for automated mineral mapping. These include but are not limited to Zeiss Mineralogic, FEI MAPS Mineralogy or QEMSCAN, TESCAN TIMA or JKMRC/FEI Mineral Liberation Analyser (Gu, 2003), which are based on SEM-EDS data, as well as Bruker M4 Tornado AMICS, which is based on micro-XRF data. Readers should refer to Table S1 for detailed descriptions of these methods and how the underlying physics have been exploited for spatial mapping and identification of minerals. While these advancements have been demonstrated to be effective, the approaches rely heavily on inferred stoichiometry to interpret mineral phases and not on crystallographic measurements. The missing crystalline information may result in indistinguishable minerals of similar chemistry, or misidentification of solid solutions. Benchtop or conventional electron- and x-ray-based methods also fall short on resolution and sensitivity when compared to higher energy techniques such as synchrotron beamlines.

Over the past decade, synchrotron facilities and their beamlines have made available coupled configurations of micro x-ray diffraction (μXRD) and micro x-ray fluorescence (μXRF), allowing for two-dimensional mapping of element and mineral composition at micrometer spatial resolutions. X-ray microprobes that house both μXRF and μXRD detectors with high count rates, short acquisition times, and rastering stages allow for opportunities to perform microscale spatial characterizations of geologic and synthetic materials (Lanzirotti et al., 2016). Unique identification of mineral phases, polymorphs, or solid solutions is best provided by XRD, a method that analyzes the diffraction patterns generated as x-rays interact with crystal planes. Identification and quantification of elements that make up a mineral phase is accomplished with XRF, a method that measures the energy of fluoresced characteristic x-rays generated from the momentary displacement of electrons. Together, the two techniques provide the unique chemical composition of an identified mineral phase. Beamlines that provide these capabilities include beamline 13-ID-E at Advanced Photon Source, beamline 4-BM at National Synchrotron Light Source II, beamline 07B2-1 at Canadian Light Source, beamline ID18F at the European Synchrotron Radiation Facility, and XFM beamline at the Australian Synchrotron. Many of these beamlines offer additional x-ray techniques, such as x-ray absorption fine structure (XAFS) and x-ray computed tomography (xCT). Access to these synchrotron facilities have opened new avenues for researchers to probe samples at high energies and resolutions, supplementing data that can be gathered from benchtop equipment such as μ-EDXRF (Nikonow and Rammlmair, 2017) or XRD which are still widely utilized for its accessibility, non-destructiveness of the sample preparation, and relatively faster collection and analysis of data.

Even with the latest advancements in coupled synchrotron techniques for micro-scale characterization, there is not yet a method of automated mineral mapping at spatial scales that are relevant in geological, environmental and earth sciences. Here, we present a new approach of 2D mineral characterization called the Synchrotron-based Machine learning Approach for RasTer (SMART) mineral mapping. The SMART mineral mapper uses machine learning in the form of an Artificial Neural Network (ANN) to build a classifier trained on coupled μXRF elemental intensities and μXRD mineral data. Applications of the trained SMART mineral mapper would require only μXRF to generate mineral maps. As such, SMART mapper addresses the fundamental problem of being limited by the time-consuming nature of XRD data acquisition and analysis for 2D characterizations of millimeter areas at micrometer resolutions.

To demonstrate this new machine learning approach, an initial classifier was developed from analysis of a sample of Eagle Ford shale rock from Texas. The μXRF and μXRD data were obtained at the Advanced Photon Source (APS) of Argonne National Laboratory, beamline 13-ID-E, which houses a hard x-ray microprobe (Lanzirotti et al., 2016; Sutton et al., 2017), and a training dataset was constructed from a small raster scan obtained at this beamline. Performance was assessed by applying the trained ANN on a reserved sample of the coupled μXRF and μXRD data which had not been included in the training data. The trained ANN was then applied to a larger scan of the same sample, i.e., self-similar upscaling. Validation was conducted by comparing the minerals identified and mapped using the SMART method to bulk powder XRD (PXRD) analysis of the Eagle Ford shale. To demonstrate the SMART method on another sample, it was applied to a known mixture formulated from six mineral standards. The mixture included minerals of similar and overlapping chemistries, which presented challenges for differentiating similar minerals and polymorphs, and testing the limits of a hard x-ray microprobe. Finally, to maximize potential for transferability of the trained SMART mineral mapper to other samples and other synchrotron data, we also addressed normalization of the input XRF intensity measurements. Potential for expansion and limitations of the methodology are also discussed.

2. The challenge of μXRD for mineral mapping and introduction to the SMART approach

Coupled μXRF-μXRD techniques are critical tools in element and mineral identification. Yet, the time-consuming nature of diffraction data acquisition and pattern analyses hinders the use of μXRD for spatial characterization of large mm-scale areas. For example, for a small, pixelated map of 0.25 mm^2 generated with a dwell time of 100 ms and spatial resolution of 2 μm per pixel, it would take approximately 2 h to collect the data, and as many as 10,417 h for a pixel-by-pixel analysis of the individual XRD patterns, given the total number of pixels at 62500 (i.e. more than one year for less than 1 square mm). This approximation assumes that analysis for a single pattern takes 10 min, which may even be an underestimation for uncharacterized samples. Such time scales are impractical and with significant human judgment required for matching of peaks to a reference database, this process is not amenable to full automation.

In light of the time constraints of relying on XRD for spatially-resolved mapping, the novel SMART mineral mapping method was developed. This approach utilizes machine learning to build a mineral classifier trained on hard x-ray synchrotron μXRF and μXRD data. The μXRF intensity data serves as the input, and the corresponding processed μXRD data serves as the coupled output. The principle behind this is that information about mineral phases is embedded in XRF data because intensities of fluoresced x-rays are sensitive to concentrations of individual elements as well as to densities of the mineral phase that is present. This is an important point, as this is not just a statistical application of machine learning; it is one based on physics. A schematic of the overall approach of data acquisition and interpretation for generating a training dataset is shown in Fig. 1.

For a single pixel, the left box in Fig. 1 summarizes the μXRD data flow where the result is a binary measure of presence or absence of each mineral. This approach allows for multiple minerals per pixel, which can

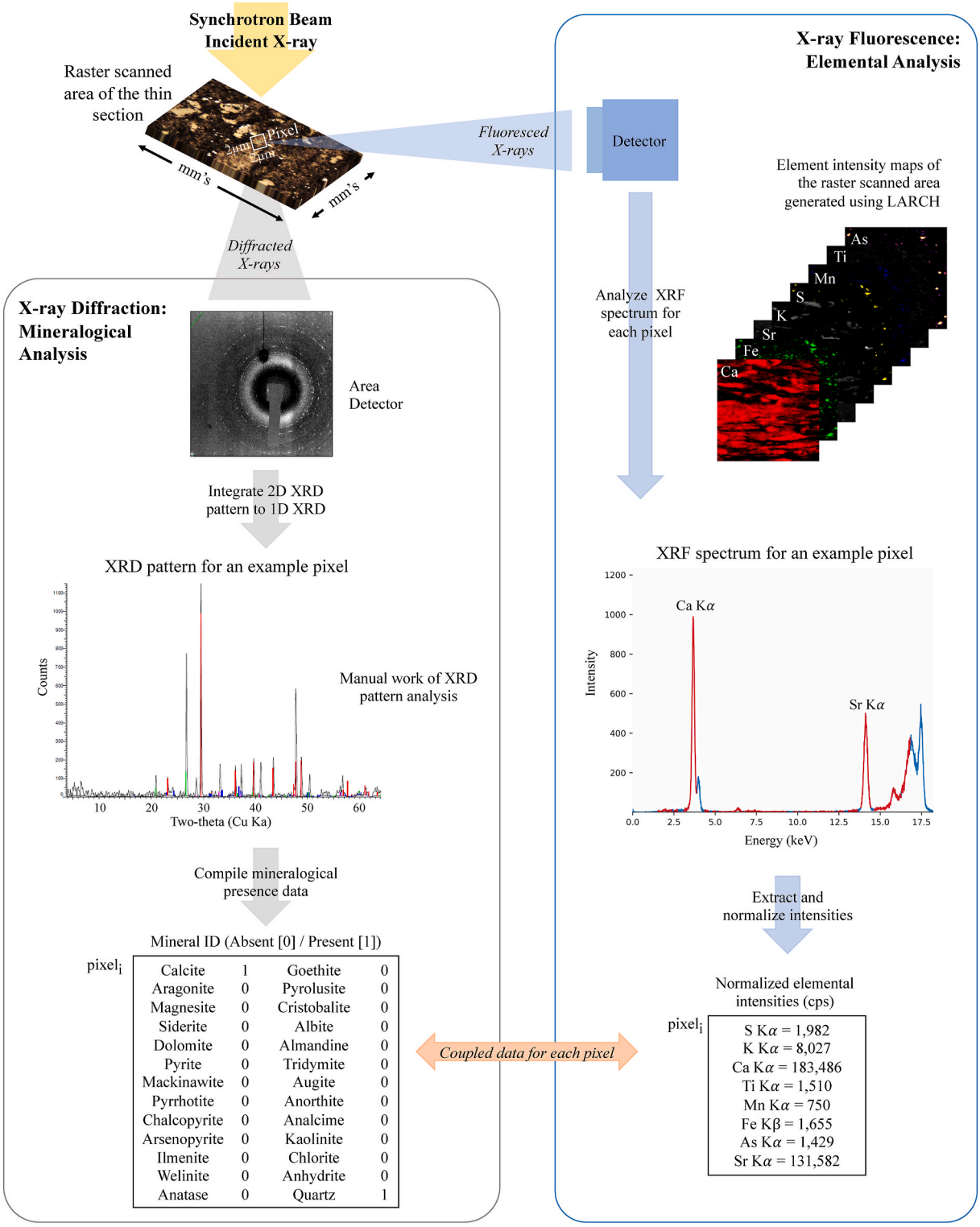

Fig. 1. The methodology for acquisition of data for training of the classifier in the SMART mineral mapping approach.

happen if the spatial resolution is coarser than the grain size. The right box in Fig. 1 summarizes the XRF data flow, summarizing extraction of intensities of eight elements selected, S, K, Ca, Ti, Mn, Fe, As, and Sr, which are constituent elements making up many common minerals. Other elements, such as Mg or Na, are not included as these are not detectable using a hard x-ray microprobe. The XRF data flow results in an array of normalized intensities for each element which is proportional to the concentration of the element in the sample. The normalization step is important because the ultimate goal is to have a SMART mineral mapper that can be applied to new μXRF scans, collected on different geological samples, at different synchrotron x-ray microprobes, by different researchers. To achieve this transferability, the data must be normalized to sample and beamline factors that are not related to mineral features. This is further addressed in Section 3.3.

Once the coupled training data are collected, training of the SMART mapper is done using an ANN, which is a type of supervised machine

learning that learns from a coupled dataset of inputs and known outputs and builds a mathematical model by extracting relationships from the data (Haykin, 2009). Using a trained SMART mineral mapper would effectively minimize the manual work of numerous XRD pattern analyses for every pixel in the sample scan. This is clearly advantageous because μXRF data are relatively fast to collect and interpret. The ANN depicted in Fig. 2 shows a simplified graphical representation of a feed-forward neural network with one hidden layer. Details about the functions and architecture of the neural network used in this work are presented in Section 4.1, and a summary of the overall workflow of the SMART mapping approach can be found in the supplementary material.

3. Materials and data

3.1. Samples

The Eagle Ford shale is a sedimentary rock formation covering much of Texas and the sample originates from an oil rich region in western Texas. Specimens were purchased from Kokurec Industries and the rock sample studied exhibited unique banded calcite mineralogy as well as nodular grains of small pyrite and large calcite grains throughout the matrix. Published mineralogical characterizations of Eagle Ford shale samples noted the abundance of calcite and quartz, as well as some pyrite and minor clay mineral phases such as kaolinite or illite (Kreisserman and Emmanuel 2018; Spokas et al., 2018). The Eagle Ford shale sample studied in this work has 3 dominant phases. This specimen served as a mineralogically simple model material for demonstration of this new methodology and for validation. For this work, the sample of this shale was thin-sectioned to 30 μm and mounted on a high-purity Suprasil 2A quartz glass slide (Spectrum Petrographics, Vancouver, WA, U.S.A.). A part of the sample was also prepared as powder for validation with bulk XRD analyses.

In addition, a mineral mixture was formulated from 6 different mineral standards, calcite, aragonite, dolomite, pyrite, pyrrhotite, pyrolusite, for the purpose of model application and validation. Calcite and aragonite are two polymorphs of calcium carbonate (same chemistry but different crystalline structures), and dolomite is a carbonate mineral that includes magnesium, an element that is not detectable with hard x-rays. The three carbonate phases are important to distinguish as they exhibit different dissolution, precipitation, and crystal growth kinetics (Busenberg and Plummer, 1986; De Choudens-Sanchez and Gonzalez, 2009; Nogues et al., 2013). Similarly, pyrite and pyrrhotite are two minerals of very similar chemistry, but with different molar ratios, different kinetics of reactions, and different known interactions with toxic elements like arsenic (Kalonji-Kabambi et al., 2020; Yang et al., 2017). The mixture was prepared by grinding to grain sizes ranging from 10 μm to 200 μm and combining equal amounts of the 6 minerals. It was prepared as a flat sample encased between pieces of Kapton® polyimide tape.

3.2. Data acquisition

The thin-sectioned shale sample and the mineral mixture were scanned at APS beamline 13-ID-E (GSECARS) using the x-ray microprobe with an incident beam energy of 18 keV, allowing for fluorescent detection of elements down to the sulfur Kα peak at 2.309 keV. A randomly selected 500 μm by 500 μm area, identified as EFS1, was scanned at 2 μm resolution. This scan consisted of 62500 pixels and for each pixel, coupled μXRF-μXRD data were collected using high-speed detectors (Lanzirotti et al., 2016; Sutton et al., 2017; Sutton and Newville 2014). With a 100 ms dwell time, the total scan time was approximately 2 h. Individual XRD patterns for each pixel were automatically generated using Larch, a data analysis tool developed at GSECARS for fluorescence, diffraction and x-ray absorption fine-structure analyses (Newville 2013).

An optical camera image of EFS1 is presented in Fig. 3a, which shows

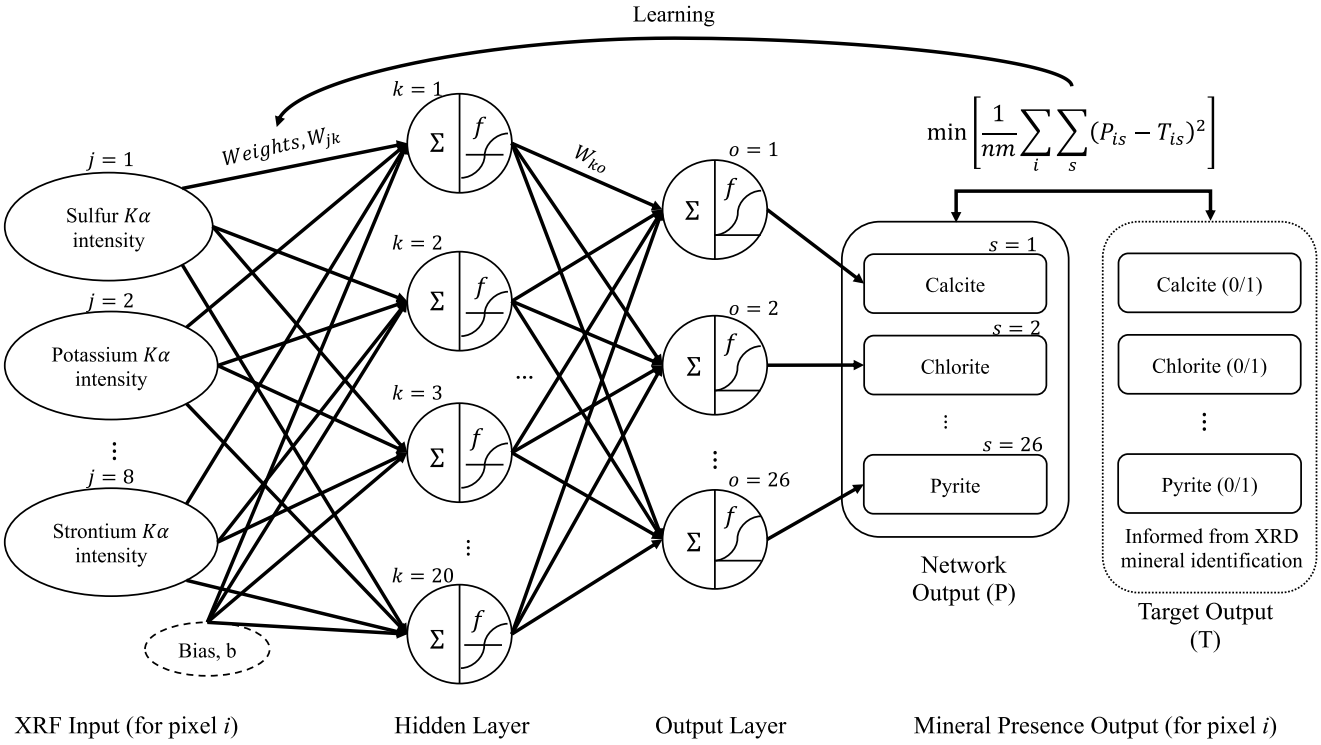

Fig. 2. Schematic of the training scheme for an Artificial Neural Network (ANN) in the SMART mineral mapper. This ANN is depicted with 1 hidden layer (for graphical simplicity) where k is the index for neurons in the hidden layer, j is the input attribute index (8 element XRF intensities) and s is the output attribute index. P is the network prediction and T is the target output (known). The learning process involves updating the weights, all W_{jk} and W_{ko}, by fitting the predictions to the targets. Variable n is the total number of data pixels and m is the total number of minerals.

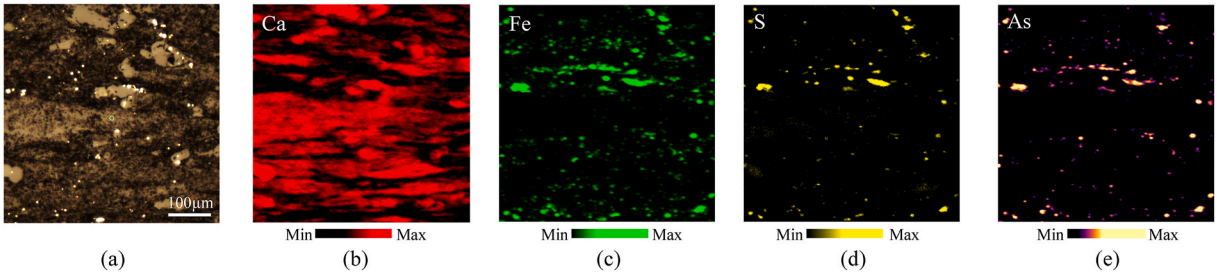

Fig. 3. (a) Optical camera image of the 500 μm × 500 μm area (EFS1) from the Eagle Ford shale thin section. (b–e) Four of the eight element intensity maps (calcium, iron, sulfur and arsenic) of EFS1 with a 2 μm resolution.

the texture of the rock. Shown in Fig. 3b–e are the element intensity maps of four selected elements, calcium, iron, sulfur and arsenic, respectively, generated using pre-normalization μXRF data. Maps of four other elements are presented in Fig. S1 of the supplementary material. All maps were generated using Larch.

For self-similar upscaling, a 7 mm by 2 mm area identified as EFS2 was scanned at a lower 4 μm resolution with a 20 ms dwell time, with only μXRF data collected. This scan consisted of 875,000 pixels which took approximately 5.5 h to obtain. Lastly, an 800 μm by 800 μm area from the mineral mixture was scanned at a 5 μm resolution, and coupled μXRF-μXRD data were collected for a total of 25,600 pixels under the same conditions as EFS1. The total time for the mineral mixture scan was approximately 1 h. See Section S1 in the supplementary material for element maps of the mineral mixture and for more details on data acquisition.

3.3. SMART mineral mapper transferability and data normalization

In this section, the expression used to normalize XRF data for transferability of the SMART mineral mapper to various samples is presented. In addition to adopting the presented methodology for self-similar upscaling, there is also the potential for application of the trained mapper to other samples. According to Sutton et al. (2002), a measured fluorescence intensity for each element is a function of concentration as well as sample thicknesses, density, physical detector configuration, detector efficiencies, incident intensity, extent of x-ray absorption, and various other instrument- and sample-dependent parameters. The theoretical expression for measured intensity presented in Sutton et al. (2002) was used as the starting point in obtaining the following simplified data normalization expression,

$$C_i = -\frac{I_i}{qRI_f}\ln\left(1-\frac{I_f}{I_0}\right) \quad (1)$$

where i denotes element i, I_f is the measured total output intensity, R is the beam path length which is related to the sample thickness, I_0 is the incident beam intensity, and q is a condensed variable consisting of detector-specific parameters, fluorescence yield, and photoelectric cross section variables that were assumed to be nearly constant for an element across different scans. This expression relates concentration to measured intensity and is written only as a function of measurable quantities. For the full derivation of Eq. (1), an explanation for assumptions or simplifications, and a discussion of the effects of self-absorption and density effects on fluorescence counts, readers should refer to Section 2 of the supplementary material.

3.4. Generating the coupled μXRF- μXRD data

For 7 of the 8 elements in the input data, the Kα emissions were utilized and only for iron, Kβ emissions were utilized to reduce the effects of the nearly overlapping fluorescence energies of manganese Kβ and iron Kα. Intensities of the 8 elements extracted from the μXRF data for each pixel were normalized using the full normalization expression presented in Eq. (1), to account for mineral-dependent absorption effects, thickness, and I_0 fluctuations, which varied in the three scans considered in this work. Larch (Newville 2013) software's capabilities to subtract pile-up effects and background, and to identify commonly overlapped peaks were utilized to further manipulate and treat the μXRF data.

For each pixel, the binary mineral variable, presence (1) or absence (0) of each mineral phase, was determined from the μXRD data. The XRD pattern covered a wide range of 2θ, up to 82° (Cu Kα), achieving detection of many reflections. Mineral identification was done using a peak matching software, MATCH! (Crystal Impact), and 26 potential mineral phases were checked for in each XRD pattern. This was done assuming no *a priori* knowledge of the mineral composition of a sample. Some of the criteria used in generating the 26-mineral list included common shale mineralogy, commonly co-located minerals, and polymorphs. In an attempt to cross-check the minerals identified and as a final step, μXRD analyses were compared against bulk PXRD data.

4. Machine learning: training, validation, and application

4.1. Training of the Artificial Neural Network (ANN) using the EFS1 scan data

From the EFS1 scan, a set of 192 pixels were randomly selected to serve as the coupled dataset. Of these, 60 % were used for training, with remaining 40 % reserved for validation and performance assessment. The ANN was built using the neural network toolbox of MATLAB® (MathWorks), and it was configured with 2 hidden layers each with 20 neurons. Sensitivity analysis on the number of neurons and hidden layers was done to find this optimal network architecture that minimized training complexity and maximized performance. The network is also built with hyperbolic tangent activation functions, a sigmoid transfer function, a mean squared error (MSE) cost function, and is based on the Levenberg and Marquardt (LM) weight updating method. We note that use of a sigmoid transfer function allowed for output of a continuous variable between 0 and 1, which added rich information about the abundance or likelihood of the presence of a mineral. Multiple early stopping criteria (i.e. minimum gradient, maximum number of training iterations, increase in the error) were set in order to avoid overfitting. The MSE evolution during training was continuously monitored and used to determine an appropriate stopping point for training (Fig. S6 in supplementary materials).

4.2. Performance metrics and assessment

To validate the trained network, the accuracy of the trained network was assessed using the reserved 76 pixels. For each mineral in each pixel, the coefficient of determination, misclassification percentages, as well as type 1 and type 2 errors were calculated. Type 1 errors correspond to false positive predictions while type II errors correspond to false negative predictions. To demonstrate the accuracy of the trained network,

performance on the testing dataset for three minerals is reported in Table 1.

As shown in Table 1, one of 76 testing pixels was mislabeled as containing calcite (false positive output), while two of 76 testing pixels were mislabeled as having no pyrite (false negative output). The overall accuracies for calcite, pyrite and quartz were calculated to be 98.7 %, 97.4 %, and 100 %, respectively, which highlights the SMART mapper's strong capabilities in predicting for the minerals present and their spatial distributions. Variable performance in the three minerals can be attributed to either the differences in the number of training pixels marked present for each mineral phase or the presence of chemically complex phases (for e.g. Mg- or Fe-rich calcite) for which the SMART mapper has not been trained on.

4.3. Application of trained network

Once the training, testing and performance evaluations were completed, the trained network was applied on the entire area of EFS1. Fig. 4a shows a three-element map of calcium, iron and sulfur, based on the μXRF data. Fig. 4b through 4e show the resulting output of the SMART mineral mapper, and the 500 μm by 500 μm mineral maps required only a few seconds to generate. Fig. 4b shows a three-color mineral map with calcite, pyrite and quartz, and such map is analogous to what one would obtain from commercially available software such as QEMSCAN. To produce this multimineral map from the SMART mapper, co-presence of minerals in a single pixel was disregarded, and the mineral with a network output value closest to 1 was assigned to that pixel. For example, in pixel (0,38), the output values for pyrite and quartz were 0.7084, and 0.9042, respectively, and therefore, pyrite was disregarded in this pixel, and quartz was marked present in the multimineral map (Fig. 4b). Fig. 4c through 4e show individual mineral maps of calcite, pyrite and quartz. These single mineral maps were generated using the continuous output variable, which allowed gradation to indicate abundance or likelihood of the mineral for each pixel, and the graded single-mineral maps also allowed for co-occurrence of minerals in a single pixel. Single maps also highlight that areas rich in calcium (which are red in Fig. 4a) are consistently labelled as calcite, and areas rich in iron (green in Fig. 4a) are marked as pyrite. Quartz presence seems to be dominant in pixels rich in neither calcium nor iron but are also found to be coexisting with calcite and pyrite in many pixels.

4.4. Demonstration of self-similar upscaling using EFS2

The self-similar area EFS2 was used to demonstrate application of the EFS1-trained SMART mineral mapper and upscaling abilities to larger, mm-scale scan areas. EFS2 was mapped without any additional training data generation or XRD analyses. Fig. 5a shows a 3-element XRF map capturing distribution of dominant elements, while the complete 8-element XRF dataset was the input to the SMART mapper. Fig. 5b shows the predicted multimineral map and Fig. 5c through 5e present the individual calcite, pyrite and quartz distribution maps.

Unique macro- and micro-scale features like sedimentary bedding layers were effectively captured in the millimeter scale mineral maps. These features are also distinguishable by eye and clearly seen in petrographic images taken of the Eagle Ford shale (Fig. S8). The micron resolution of the mineral maps allowed for fine-scale characterizations and differentiation of the large nodular calcite grains from the small pyrite grains. No additional times except for the XRF data acquisition time were needed in spatially characterizing EFS2 because times for SMART mapper application and map generation are negligible.

Table 1
Performance of trained network on reserved testing data. Misclassification is the percentage of total false predictions out of 76 testing pixels.

Mineral	R-Squared	Misclassification (%)	Type I Error Count (out of 76)	Type II Error Count (out of 76)
Calcite	0.937	1.3	1	0
Pyrite	0.903	2.6	0	2
Quartz	0.999	0	0	0

4.5. PXRD-based validation and semiquantitative analysis

In order to further validate the minerals identified in the Eagle Ford shale using the SMART mineral mapper, powdered samples were analyzed using the high-resolution synchrotron PXRD at the 11-BM beamline at APS. Readers should refer to Section S5 in the supplementary material for details about the beamline setup and configuration, and the labelled PXRD pattern. From the analyses of four replicate samples, calcite, quartz and pyrite were identified, along with some unidentified peaks near 12–15° (Cu Kα). Based on previous study of the Eagle Ford shale by some of the authors, these peaks are likely originating from Kaolinite ($Al_2Si_2O_5(OH)_4$) (Spokas et al., 2018).

In addition to mineral identification, semiquantitative analyses were conducted on the PXRD data and the generated maps via pixel counting and converting to weight percentages based on the mineral densities. Table 2 summarizes the quantitative results from the generated mineral maps of EFS1 and EFS2, along with results from quantitative PXRD analysis of powdered Eagle Ford shale samples (4 replicates). Values of standard error (SE) of the mean are also reported for each mineral in the PXRD data and the small SE values indicate reasonably precise measurements of PXRD quantification.

Results from the pixel counting approach for mineral quantification on EFS1 and EFS2 indicate an overall trend in calcite being the most dominant mineral, followed by quartz, and pyrite. This general trend is also consistently seen in the PXRD case. Calcite was slightly underestimated in the pixel counting approach, while pyrite and quartz were slightly overestimated in the pixel counting approach. However, the observed differences in weight percentages are reasonable, given the comparison of quantifications from thin sections and powdered rock samples.

Approximately 6% of the pixels in both EFS1 and EFS2 were left unidentified, indicating presence of a fourth mineral phase or pore space. Informed by the PXRD results, it can be predicted that the some of the unidentified pixels correspond to kaolinite. Because kaolinite peaks were not clearly identified in the integrated XRD patterns from the EFS1 XRD data, no training pixels included kaolinite labels. The missing kaolinite peaks can be attributed to three possible reasons: 1) small kaolinite peaks are masked by a large hump between 2θ of 11°–30° (Cu Kα) in the integrated XRD pattern, which originates from the glass substrate of the thin section, 2) kaolinite peaks are masked by a more dominant co-occurring phase, or 3) there is dominance of kaolinite reflections in the lower and undetectable region of the 2θ range.

With the presence of unlabeled pixels, the differentiation and labelling of quartz is further emphasized since both types of data points are considered blank in terms of the detectable elemental presence in the XRF data of 8 elements. However, as previously mentioned, the measured intensity is not only a function of element concentrations but also the mineral phase densities and the resulting extent of attenuation. Thus, the differences in the number of photons that fluoresce from a spot consisting of quartz and a spot consisting of no minerals were captured by the neural network, leading to clear identification of quartz in the Eagle Ford shale sample.

4.6. Mineral mixture for further demonstration and similar mineral differentiation

For further demonstration of the capabilities of the SMART mineral mapper, a new network (hereafter referred to as 'mixture-trained network') was trained using data from the mineral mixture. Training was done following the aforementioned training steps. Fig. 6 shows the

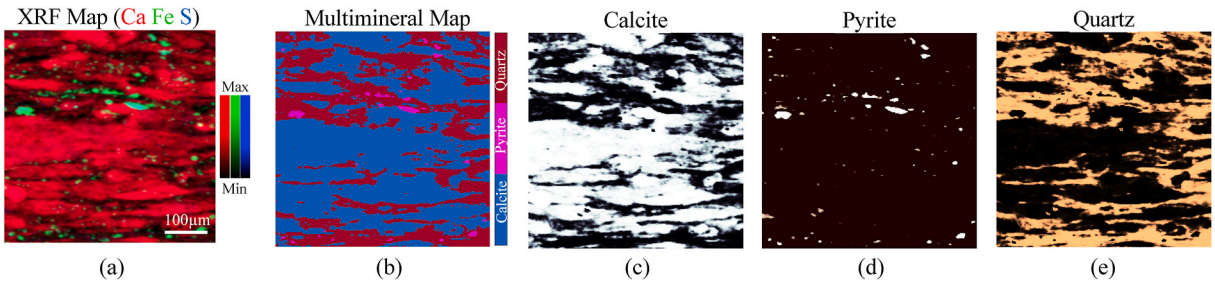

Fig. 4. Eagle Ford shale (a) three-element XRF map of the EFS1 area (0.25 mm^2) indicating calcium, iron and sulfur intensities; (b) a multimineral map of the three primary minerals, calcite, pyrite and quartz, with a 2 μm resolution, and; (c–e) single mineral maps for each mineral where black represents no presence in all three maps.

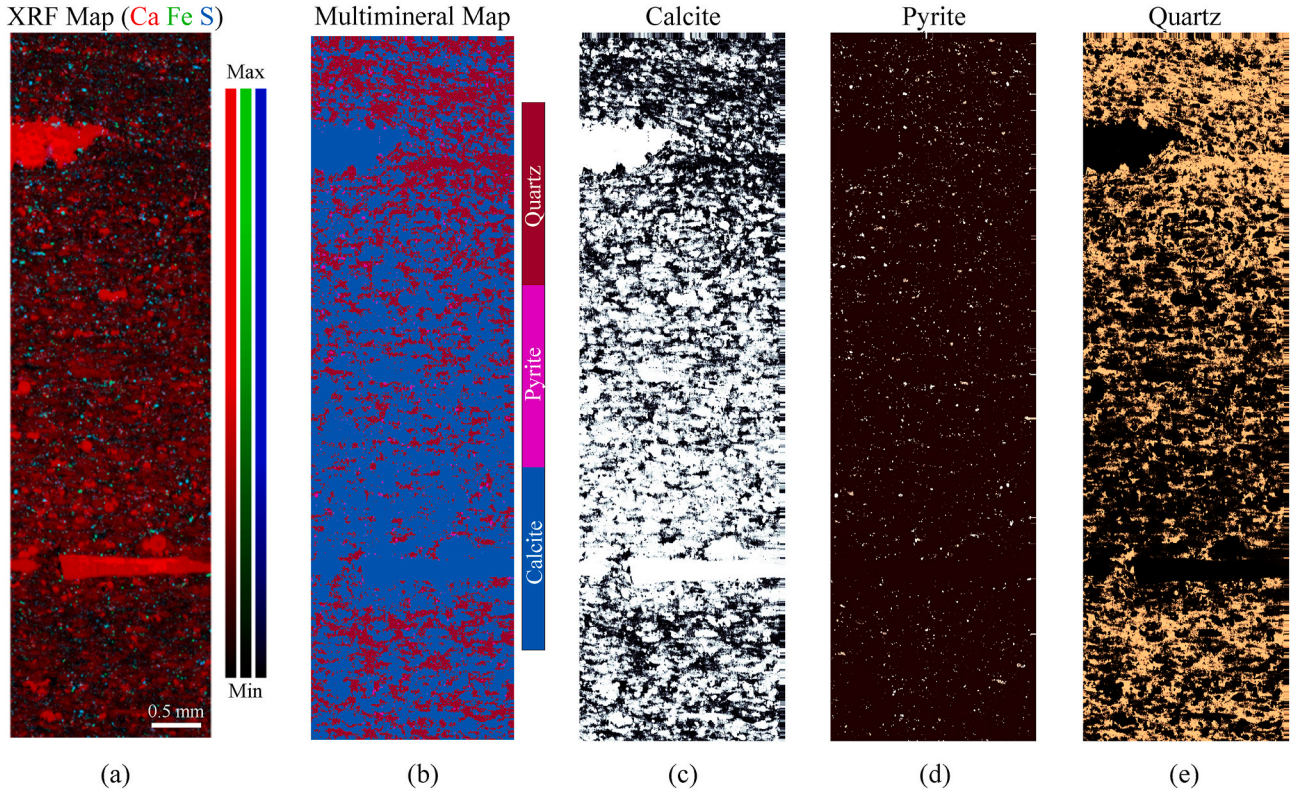

Fig. 5. Eagle Ford shale (a) three-element XRF map of the EFS2 area (14 mm^2) indicating calcium, iron and sulfur intensities; (b) a multimineral map of the three primary minerals, calcite, pyrite and quartz, with a 4 μm resolution, and; (c–e) single mineral maps for each mineral where black represents no presence in all three maps.

Table 2
Semi-quantitative analysis of EFS1, EFS2 and the powdered sample.

Mineral	Calcite	Pyrite	Quartz	Unidentified or Kaolinite
Wt. % – EFS1	58.7	2.4	32.9	6.0
Wt. % – EFS2	62.0	2.6	28.9	6.5
Wt. % from PXRD analysis ± std. error of the mean	70.7 ± 0.4	1.4 ± 0.2	25.8 ± 0.4	2.1 ± 0.7

output of the mixture-trained network, including a multimineral map and 6 individual mineral maps.

The visible trends in the mineral maps (Fig. 6) follow closely the element distributions seen in the element maps of the mineral mixture (Fig. S2). The carbonate mineral maps (Fig. 6b and 6c) show that calcite and aragonite were differentiated. This may be due to the density difference between the two phases, which was captured by the SMART mineral mapper. Secondary check of XRD patterns from some aragonite labelled and calcite labelled pixels were conducted (Fig. S9) which further verified presence of aragonite and calcite, respectively. However, unless every pixel is cross-checked with the μXRD data, the reliability of the differentiation is unquantifiable. Things are further complicated by the closeness of the density of the two calcium carbonates, and the unknown sensitivity of the fluoresced x-rays to small density variations. There is also the potential for co-presence of another mineral phase in a single pixel that further jeopardizes the dependency

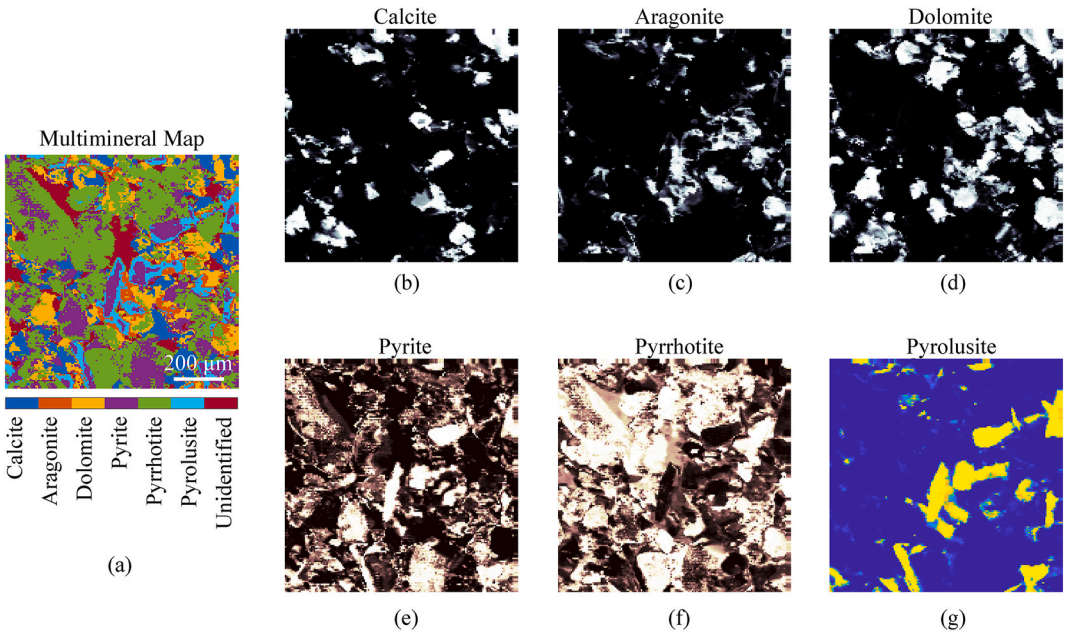

Fig. 6. Mineral mixture (a) a multimineral map of all 6 minerals, calcite, aragonite, dolomite, pyrite, pyrrhotite, and pyrolusite, and an unidentified category, with a 5 μm resolution, and; (b–g) single mineral maps for each mineral where black (b–f) or blue (g) represents no presence. (For interpretation of the references to color in this figure legend, the reader is referred to the Web version of this article.)

on density variations for polymorph differentiation. Sensitivity relating to polymorph differentiation is promising with this machine learning method, but quantifying the accuracy is still to be done and remains as future work.

A third calcium carbonate mineral, dolomite, was also distinguished (Fig. 6d) from calcite and aragonite. Dolomite chemistry differs by the presence of magnesium, which is invisible to hard x-rays. However, the clear differences in the XRD patterns, and consistent copresence of strontium with dolomite has allowed for the differentiation of this carbonate phase from chemically similar calcite and aragonite phases. A combined dolomite and strontium map (Fig. S10) highlights this high correlation between the mineral presence and the element presence. It can be predicted that the SMART mapper was able to extract out this non-trivial yet subtle relationship between the input and the output, which would have otherwise been missed in analysis of only elemental presence.

Labeling of all iron rich spots (Fig. S2) were distributed between pyrite and pyrrhotite (Fig. 6e and f), indicating the network's ability to separate out another pair of minerals that are nearly impossible to distinguish and identify only based on chemistry. With the use of a coupled μXRF-μXRD dataset containing elemental and density variation information and a corresponding mineral label, the SMART mineral mapper is able to capture, to some extent, distributions of polymorph or similar minerals, although this remains to be analyzed in greater depths in future works.

5. Discussion and conclusion

5.1. Analysis of the SMART mineral mapping approach

For the first time, a method of spatial mineral mapping was developed based on machine learning interpretation of data from the synchrotron x-ray microprobe techniques of μXRF and μXRD. Performance of the SMART mineral mapper was demonstrated using datasets from a natural shale rock and a known mineral mixture. This approach is different from purely element-stoichiometry based approaches for mineral mapping because the SMART mapper includes XRD, which provides definitive mineral identification based on crystal structure. This is especially important for samples with coexistence of minerals with similar chemistry like pyrite and pyrrhotite, or dolomite and other calcium carbonates.

The detection of multiple minerals per pixel was achieved via the SMART mineral mapper and observed in the mineral maps of EFS1, EFS2, and the mineral mixture. This capability is advantageous in getting a more complete picture of the rock or mixture mineralogy. Depth-averaged mineralogical information and coarser spatial resolution than observed grain sizes resulted in a more complex training dataset from which the neural network learned from. Through sufficient training, the network was able to effectively extract out the relationships between specific elements (or a set of elements) to a mineral phase (or a set of phases).

While the SMART mapping approach still uses XRD data, the machine learning aspect minimizes the dependence on XRD and therefore minimizes the times needed to mineralogically map samples. These principles are visualized in Fig. 7, which presents an estimated total time required for mineral mapping using the SMART method plotted against sample area. Also shown are the estimated total times that would be hypothetically required for a pixel-by-pixel approach if one were to analyze both μXRF and μXRD data for an entire sample at high resolution.

Fig. 7 shows that in a pixel-by-pixel approach of XRD pattern analysis (blue-diamond line), mapping mm-sized areas would take numerous years, which is clearly unfeasible. In contrast, the SMART machine learning approach shows significant reductions in time (green-triangle line) and the times to acquire and analyze data, initially train a neural network, and mineralogically map samples are quite reasonable for a wide range of areas. Subsequently, total times required for application of an already-trained network (red-circle line) can simply be approximated by the XRF data acquisition times. For example, the time frame for training and applying the SMART mineral mapper to mineralogically map a 10 mm^2 map at 2 μm resolution (2,500,000 pixels) is approximately 52 h, which comes from 2 h needed for μXRF-μXRD data acquisition from a small area, 33 h for subsequent data analysis (i.e., XRD peak matching and XRF data extraction), and 17 h for XRF data acquisition from the 10 mm^2 area. The 33 data analysis hours do not need to be accounted for again in the case of upscaling or direct

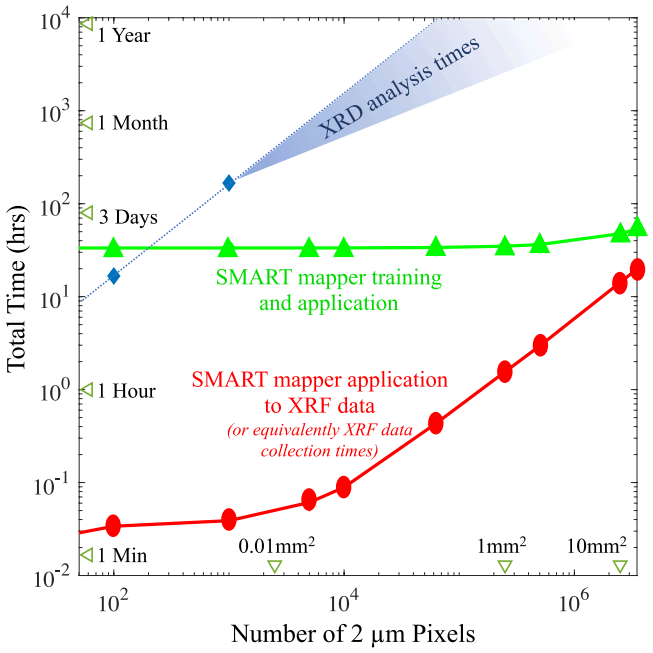

Fig. 7. Plot of time vs number of pixels (or area) for the SMART mapper application with training in green (triangles), direct SMART mapper application to XRF data in red (circles), and for a hypothetical pixel-by-pixel approach in blue (diamonds). This analysis assumes image resolution of 2 µm, 200 coupled data point analyses for mapper training, 10 min to analyze a single XRD pattern, and XRF dwell times of 20 ms. (For interpretation of the references to color in this figure legend, the reader is referred to the Web version of this article.)

application of the trained mapper, and the total time is reduced to 17 data acquisition hours to map a new 10 mm^2-sized area. These time frames allow for collection of multiple mm-sized XRF-only scans (which can be later mineralogically mapped), because a synchrotron beam cycle is typically 3–4 days.

5.2. Limitations and improvements

Using data from a hard x-ray source, there is a lack of information on lighter elements like Na, Mg, Al and Si, which are common constituents of minerals in natural settings. This means that reliability of identifying minerals composed solely of those elements in lowered, and quantification of the elemental composition in minerals like calcium silicate hydrates with variable calcium to silica ratios or solid solutions composed of lighter elements cannot be done (Plattenberger et al., 2019). While the hard x-ray microprobe was appropriate for analyses of samples studied in this work, it may be beneficial to consider beamlines that utilize x-rays in the tender or soft regimes to study samples with minerals composed of lighter elements or samples rich in clays.

In the data analysis and training data acquisition stages, some complexities may arise depending on sample composition and the elements chosen as part of the training due to spectral overlaps. There exist some unavoidable µXRF spectrum overlaps such as Mn Kβ and Fe Kα or Fe Kβ and Ni Kα, which cannot be resolved due to the resolution of the detectors. Judicious selection of the elements and emission lines should be made, as was done in this work (i.e., choice of Mn Kα and Fe Kβ as the input data). Additional discussions on other instrumental overlaps can be found in the supplementary material Section S7.

Using µXRD to classify ill-ordered crystalline phases is unreliable, which limits application of the SMART mapping approach to crystalline materials and samples. Amorphous phases often exhibit widened peaks or humps in an XRD pattern, and these non- or partially-crystalline phases are common in materials like cement pastes composed mainly of newly precipitated phases. Samples such as these would require other methodologies for characterization. See, for example, work of Gaboreau et al. (2017), for their chemical and mineralogical characterizations of specialized concrete formulations.

While the methodology presented here shows an 8 element and 3 or 6 mineral SMART mappers, the approach can be built up to include other elements such as copper, lead, mercury, etc., and additional mineral labels. Reformatting of the input and output data pair and adapting of the methodology can be achieved on new natural and synthetic materials. Although SMART mineral mapping is not without limitations, there are positive prospects for pooling coupled datasets from multiple samples or combining datasets from hard, tender, soft, or even 3D x-ray beamlines to achieve extended SMART mineral mapping. Generated maps can be further utilized in geochemical reactive transport modeling, as such a tool requires precise parameterization of thermodynamic stability, kinetics of reactions, and morphological and surface area evolution all of which are driven by mineralogical composition and spatial distribution.

Declaration of competing interest

The authors declare that they have no known competing financial interests or personal relationships that could have appeared to influence the work reported in this paper.

Acknowledgements

This material is based upon work supported by the High Meadows Environmental Institute at Princeton University. Portions of this work were performed at GeoSoilEnviroCARS (The University of Chicago, Sector 13), Advanced Photon Source (APS), Argonne National Laboratory. GeoSoilEnviroCARS is supported by the National Science Foundation – Earth Sciences (EAR – 1634415) and Department of Energy-GeoSciences (DE-FG02-94ER14466). This research used resources of the Advanced Photon Source, a U.S. Department of Energy (DOE) Office of Science User Facility operated for the DOE Office of Science by Argonne National Laboratory under Contract No. DE-AC02-06CH11357. Use of the Advanced Photon Source at Argonne National Laboratory was supported by the U. S. Department of Energy, Office of Science, Office of Basic Energy Sciences, under Contract No. DE-AC02-06CH11357. The authors acknowledge the use of Princeton's Imaging and Analysis Center, which is partially supported by the Princeton Center for Complex Materials, a National Science Foundation (NSF)-MRSEC program (DMR-1420541).

Appendix A. Supplementary data

Supplementary data to this article can be found online at https://doi.org/10.1016/j.cageo.2021.104898.

Computer code and data availability

Data and computer code are available and accessible on Digital Rocks Portal (Prodanovic et al., 2015), as project "Eagle Ford Shale: Synchrotron-Based Element and Mineral Maps" (Peters and Kim, 2020). [https://www.digitalrocksportal.org/projects/258].

Software required

Larch (Newville 2013), MATLAB.

Program language

MATLAB.

Program/data size

1.2 GB (EFS1), 7.1 GB (EFS2), 3.9 MB (sample input data), 11.1 MB (trained neural network), and 3.5 KB (MATLAB script for data reading).

Instructions

See project data branches in Digital Rocks Portal for detailed instructions.

Authorship statement

Julie J. Kim: Conceptualized the machine learning approach, collected synchrotron data, conducted the data analysis, produced the machine learning results, wrote, revised, and edited the paper. **Florence T. Ling**: Collected synchrotron data, provided expert guidance on data interpretation, revised and edited the paper. **Dan A. Plattenberger**: Collected synchrotron data, provided expert guidance on data interpretation, revised and edited the paper. **Andres F. Clarens**: Collected synchrotron data, provided expert feedback on results and discussions. **Antonio Lanzirotti**: Provided expert guidance on synchrotron x-ray spectroscopy and data interpretation, revised and edited the paper. **Matthew Newville**: Provided expert guidance on synchrotron x-ray spectroscopy and data interpretation. **Catherine A. Peters**: Served as advisor author, conceptualized the machine learning approach, collected synchrotron data, provided expert feedback on data interpretation, methods, results and discussions, revised and edited the paper.

References

Basile-Doelsch, I., Amundson, R., Stone, W.E.E., Masiello, C.A., Bottero, J.Y., Colin, F., Masin, F., Borschneck, D., Meunier, J.D., 2005. "Mineralogical control of organic carbon dynamics in a volcanic ash soil on La Reunion". Eur. J. Soil Sci. 56, 689–703.

Beckingham, L.E., Mitnick, E.H., Steefel, C.I., Zhang, S., Voltolini, M., Swift, A.M., Yang, L., Cole, D.R., Sheets, J.M., Ajo-Franklin, J.B., DePaolo, D.J., Mito, S., Xue, Z., 2016. Evaluation of mineral reactive surface area estimates for prediction of reactivity of a multi-mineral sediment. Geochem. Cosmochim. Acta 188, 310–329.

Beckingham, L.E., Steefel, C.I., Swift, A.M., Voltolini, M., Yang, L., Anovitz, L.M., Sheets, J.M., Cole, D.R., Kneafsey, T.J., Mitnick, E.H., Zhang, S., Landrot, G., Ajo-Franklin, J.B., DePaolo, D.J., Mito, S., Xue, Z., 2017. "Evaluation of accessible mineral surface area for improved prediction of mineral reaction rates in porous media". Geochem. Cosmochim. Acta 205, 31–49.

Bensinger, J., Bekingham, L.E., 2020. "CO2 storage in the Paluxy formation at the Kemper County CO2 storage complex: pore network properties and simulated reactive permeability evolution". It. J. Greenhouse Gas Contr. 93, 10287.

Bourg, I.C., 2015. Sealing shales versus brittle shales: a sharp threshold in the material properties and energy technology uses of fine-grained sedimentary rocks. Environ. Sci. Technol. Lett. 2 (10), 255–259.

Busenberg, E., Plummer, L.N., 1986. A comparative study of the dissolution and crystal growth kinetics of calcite and aragonite. In: Mumpton, F.A. (Ed.), Studies in Diagenesis, vol. 1578. USGS, pp. 139–168.

De Choudens-Sanchez, V., Gonzalez, L.A., 2009. Calcite and aragonite precipitation under controlled instantaneous supersaturation: elucidating the role of CaCO3 saturation state and Mg/Ca ratio on calcium carbonate polymorphism. J. Sed. Res. 79 (6), 363–376.

Deng, H., Fitts, J.P., Crandall, D., McIntyre, D., Peters, C.A., 2015. Alterations of fractures in carbonate rocks by CO2-acidified brines. Environ. Sci. Technol. 49 (16), 10226–10234.

Deng, H., Fitts, J.P., Peters, C.A., 2016. Quantifying fracture geometry with X-ray tomography: technique of iterative local thresholding (TILT) for 3D image segmentation. Comput. Geosci. 20, 231–244.

Deng, H., Peters, C.A., 2019. Reactive transport simulation of fracture channelization and transmissivity evolution. Environ. Eng. Sci. 36 (1), 90–101.

Deng, H., Fitts, J.P., Tappero, R.V., Kim, J.J., Peters, C.A., 2020. Acid erosion of carbonate fractures and accessibility of arsenic-bearing minerals. In: Operando Synchrotron-Based Microfluidic experiment." Environmental Science and Technology, vol. 54, pp. 12502–12510, 19.

Ehlert, K., Mikutta, C., Jin, Y., Kretzschmar, R., 2018. Mineralogical controls on the bioaccessibility of arsenic in Fe(III)–As(V) coprecipitates. Environ. Sci. Technol. 52 (2), 616–627.

Ellis, B.R., Fitts, J.P., Bromhal, G.S., McIntyre, D.L., Tappero, R., Peters, C.A., 2013. Dissolution-driven permeability reduction of a fractured carbonate caprock. Environ. Eng. Sci. 30 (4), 187–193.

Ellis, B.R., Peters, C.A., 2016. 3D Mapping of calcite and a demonstration of its relevance to permeability evolution in reactive fractures. Adv. Water Resour. 95, 246–253.

Fang, Y., Elsworth, D., Wang, C., Jia, Y., 2018. Mineralogical controls on frictional strength, stability, and shear permeability evolution of fractures. J. Geophys. Res.: Solid Earth 123, 3549–3563.

Fitts, J.P., Peters, C.A., 2013. Caprock fracture dissolution and CO2 leakage. Rev. Mineral. Geochem. 77 (1), 459–479.

Gaboreau, S., Prêt, D., Montouillout, V., Henocq, P., Robinet, J.-C., Tournassat, C., 2017. Quantitative mineralogical mapping of hydrated low pH concrete. Cement Concr. Compos. 83, 360–373.

Glassley, W.E., Simmons, A.M., Kercher, J.R., 2002. Mineralogical heterogeneity in fractured, porous media and its representation in reactive transport models. Appl. Geochem. 17, 699–708.

Golab, A., Romeyn, R., Averdunk, H., Knackstedt, M., Senden, T.J., 2013. 3D characterisation of potential CO2 reservoir and seal rocks. Aust. J. Earth Sci. 60 (1), 111–123.

Gu, Y., 2003. Automated scanning electron microscope based mineral liberation analysis. J. Miner. Mater. Char. Eng. 2 (No. 1), 33–41.

Guntoro, P.I., Tiu, G., Ghorbani, Y., Koch, P.-H., Rosenkranz, J., 2019a. X-Ray microcomputed tomography (μCT) for mineral characterization: a review of data analysis methods. Minerals 9, 183.

Guntoro, P.I., Tiu, G., Ghorbani, Y., Lund, C., Rosenkranz, J., 2019b. Application of machine learning techniques in mineral phase segmentation for X-ray microcomputed tomography (μCT) data. Miner. Eng. 142, 105882.

Haykin, S., 2009. Neural Networks and Learning Machines, third ed. Prentice-Hall, Cambridge, MA, p. 906.

Jennings-Gray, D., Berg, S., Gargi, G., Krevor, S., 2020. Combining machine learning with dual-energy micro-ct to segment mineral phases. Goldschmidt Abstracts 1179.

Kalonji-Kabambi, A., Demers, I., Bussiere, B., 2020. Reactive transport modeling of the geochemical behavior of highly reactive tailings in different environmental conditions. Appl. Geochem. 122, 104761.

Kreisserman, Y., Emmanuel, S., 2018. Release of particulate iron sulfide during shale-fluid interaction. Environ. Sci. Technol. 52, 638–643.

Lanzirotti, A., Newville, M., Manoukian, L., Lange, K., 2016. High-speed, coupled micro-beam XRD/XRF/XAFS mapping at GSECARS: APS beamline 13-ID-E. In: The Clay Minerals Society Workshop Letters Series, 21, pp. 53–64 (Chapter 5).

Li, L., Maher, K., Navarre-Sitchler, A., Druhan, J., Meile, C., Lawrence, C., Moore, J., Perdrial, J., Sullivan, P., Thompson, A., Jin, C.I., Bolton, E.W., Brantley, S.L., Dietrich, W.E., Mayer, K.U., Steefel, C.I., Valocchi, A., Zachara, J., Kocar, B., Mcintosh, J., Tutolo, B.M., Kumar, M., Sonnenthal, E., Bao, C., Beisman, J., 2017. Expanding the role of reactive transport models in critical zone processes. Earth Sci. Rev. 165, 280–301.

Ma, J., Querci, L., Hattendorf, B., Saar, M.O., Kong, X.-Z., 2019. Toward a spatiotemporal understanding of dolomite dissolution in sandstone by CO2-enriched brine circulation. Environ. Sci. Technol. 53 (21), 12458–12466.

Maitre, J., Bouchard, K., Bedard, L.P., 2019. Mineral grains recognition using computer vision and machine learning. Comput. Geosci. 130, 84–93.

Newville, M., 2013. Larch: an analysis package for XAFS and related spectroscopies. J. Phys. Conf. 430, 2. https://doi.org/10.1088/1742-6596/430/1/012007, 012007.

Nikonow, W., Rammlmair, D., 2017. Automated mineralogy based on micro-energy-dispersive X-ray fluorescence microscopy (μ-EDXRF) applied to plutonic rock thin sections in comparison to a mineral liberation analyzer. Geosci. Instrument. Methods Data Syst. 6, 429–437.

Nikonow, W., Rammlmair, D., Meima, J.A., Schodlok, M.C., 2019. Advanced mineral characterization and petrographic analysis by μ-EDXRF, LIBS, HIS and hyperspectral data merging. Mineral. Petrol. 113, 417–431.

Nogues, J.P., Fitts, J.P., Celia, M.A., Peters, C.A., 2013. Permeability evolution due to dissolution and precipitation of carbonates using reactive transport modeling in pore networks. Water Resour. Res. 49, 6006–6021.

Peters, C.A., 2009. Accessibilities of reactive minerals in consolidated sedimentary rock: an imaging study of three sandstones. Chem. Geol. 265, 198–208.

dataset Peters, C.A., Kim, J.J., 2020. Eagle Ford shale: synchrotron-based element and mineral maps. Digital Rocks Portal. https://doi.org/10.17612/T3A6-6356. https://www.digitalrocksportal.org/projects/258.

Pirrie, D., Butcher, A.R., Power, M.R., Gottlieb, P., Miller, G.L., 2004. Rapid quantitative mineral and phase analysis using automated scanning electron microscopy (QemSCAN); potential applications in forensic geoscience. Geol. Soc. Spec. Publ. 232 (Smith 1991), 123–136.

Plattenberger, D.A., Ling, F.T., Peters, C.A., Clarens, A.F., 2019. Targeted permeability control in the subsurface via calcium silicate carbonation. Environ. Sci. Technol. 53, 7136–7144.

Pret, D., Sammartino, S., Beaufort, D., Meunier, A., Fialin, M., Michot, L.J., 2010. A new method for quantitative petrography based on image processing of chemical element maps: Part I. Mineral mapping applied to compacted bentonites. Am. Mineral. ume 95, 1379–1388.

Prodanovic, M., Esteva, M., Hanlon, M., Nanda, G., Agarwal, P., 2015. Digital Rocks Portal: a repository for porous media images. https://doi.org/10.17612/P7CC7K.

Qin, F., Beckingham, L.E., 2019. Impact of image resolution on quantification of mineral abundances and accessible surface areas. Chem. Geol. 523, 31–41.

Rahman, A., Timms, G., Shahriar, S., Sennersten, C., Davie, A., Lindley, C.A., Hellicar, A. D., Biggins, D., Coombe, M., 2016. Association between imaging and XRF sensing: a machine learning approach to discover mineralogy in abandoned mine voids. IEEE Sensor. J. 16 (No. 11).

Robinet, J.-C., Sardini, P., Coelho, D., Parneix, J.-C., Pret, D., Sammartino, S., Boller, E., Altmann, S., 2012. Effects of mineral distribution at mesoscopic scale on solute diffusion in a clay-rick rock: example of the Callovo-Oxfordian mudstone (Bure, France). Water Resour. Res. 48. W05554.

Soulaine, C., Gjetvaj, F., Garing, C., Roman, S., Russian, A., Gouze, P., Tchelepi, H.A., 2016. The Impact of sub-resolution porosity of X-ray microtomography images on the permeability. Transport Porous Media 113, 227–243.
Spokas, K., Peters, C.A., Pyrak-Nolte, L., 2018. Influence of rock mineralogy on reactive fracture evolution in carbonate-rich caprocks. Environ. Sci. Technol. 52, 10144–10152.
Spokas, K., Fang, Y., Fitts, J.P., Peters, C.A., Elsworth, D., 2019. Collapse of reacted fracture surface decreases permeability and frictional strength. J. Geophys. Res.: Solid Earth 124, 12,799–12,811.
Sutherland, D.N., Gottlieb, P., 1991. Application of automated quantitative mineralogy in mineral processing. Miner. Eng. 4, 753–762.
Sutton, S.R., Bertsch, P.M., Newville, M., Rivers, M., Lanzirotti, A., Eng, P., 2002. Microfluorescence and microtomography analyses of heterogeneous earth and environmental materials. Rev. Mineral. Geochem. 49 (issue 1), 429–483.
Sutton, S.R., Newville, M., 2014. 15.12 – synchrotron X-ray spectroscopic analysis In: Reference Module in Earth Systems and Environmental Sciences. Treatise on Geochemistry, second ed., 15, p. 213 130.
Sutton, S.R., Lanzirotti, A., Newville, M., Rivers, M.L., Eng, P., Lefticariu, L., 2017. Spatially resolved elemental analysis, spectroscopy and diffraction at the GSECARS sector at the Advanced Photon Source. J. Environ. Qual. 46, 1158–1165.
Tsuji, T., Yamaguchi, H., Ishii, T., Matsuoka, T., 2010. Mineral classification from quantitative X-ray maps using neural network: application to volcanic rocks. Isl. Arc 19 (1), 105–119.
Wang, S., Tao, Z., Persily, S.M., Clarens, A.F., 2013. CO2 adhesion on hydrated mineral surface. Environ. Sci. Technol. 47, 11858–11865.
Yang, Y., Chen, T., Sumona, M., Gupta, B.S., Sun, Y., Hu, Z., Zhan, X., 2017. Utilization of iron sulfides for wastewater treatment: a critical review. Rev. Environ. Sci. Biotechnol. 16, 289–308.
Zhang, L., Parthasarathy, H., Karamalidis, A., 2017. Investigation on arsenopyrite dissolution and as (III) migration under geologic carbon storage conditions: a numerical simulation approach. Greenhouse Gases Sci. Technol. 7, 460–473.